

Supplemental material for Multi-synchrony in active microfilaments

Yi Man and Eva Kanso*

University of Southern California, Los Angeles, CA 90089, USA

1 Single filament

We consider an elastic filament clamped at its base (Fig. S1(a)). We model the filament “activity” as a force of constant magnitude F applied at the filament tip along the local tangential direction, thus it is referred to as a follower force. The dynamics of the filament using this model has been well-studied in Ref. [1, 2]. Here we briefly review the mathematical set-up and introduce the corresponding oscillation patterns.

As with all fluidic systems in the microscopic world, we focus on low-Reynolds-number dynamics. At any local point along the filament, the instantaneous force balance satisfies

$$\mathbf{f}_h + \mathbf{f}_e = \mathbf{0}. \quad (1)$$

According to the resistive force theory, the hydrodynamic force is proportional to the velocity such that

$$\mathbf{f}_h = -\xi \left(\mathbf{I} - \frac{1}{2} \mathbf{t} \mathbf{t} \right) \cdot \mathbf{r}_t, \quad (2)$$

where $\mathbf{r}(s, t)$, a function of both time t and arc length s , represents the shape of the filament; The subscript $()_t$ denotes the time derivative; $\mathbf{t} = \mathbf{r}_s$ is the local tangential direction; the subscript $()_s$ denotes spatial derivative with respect to arc length s . Here we assumed the drag coefficient ξ along the normal direction is twice as large as that along the tangential direction [3]. We consider planar motion, in the (x, y) plane, therefore, the elastic force is given by

$$\mathbf{f}_e = -B \mathbf{r}_{ssss} + (\Lambda \mathbf{t})_s, \quad (3)$$

where B is the bending modulus; Λ is the Lagrangian multiplier enforced by the condition of inextensibility.

We nondimensionalize the variables with the longitudinal length of the filament L , and the bending relaxation time scale $\xi L^4/B$, then force balance equation Eq. (1) becomes

$$\bar{\mathbf{r}}_{\bar{t}} = (\mathbf{I} + \mathbf{t} \mathbf{t}) \cdot \left[-\bar{\mathbf{r}}_{\bar{s}\bar{s}\bar{s}\bar{s}} + (\bar{\Lambda} \mathbf{t})_{\bar{s}} \right]. \quad (4)$$

The dimensionless quantities with ‘bar’s are scaled as: $\bar{\mathbf{r}} = \mathbf{r}/L$, $\bar{t} = tB/(\xi L^4)$, $\bar{s} = s/L$, $\bar{\Lambda} = \Lambda L^2/B$. For convenience, in the following calculation, we drop the ‘bar’s to represent the dimensionless quantities. We calculate the right-hand side of Eq. (4) using Frenet-Serret frame. By introducing the local angle θ which satisfies $\tan \theta = dy/dx$, we calculate $\mathbf{r}_{ssss} = -3\theta_s \theta_{ss} \mathbf{t} + (\theta_{sss} - \theta_s^3) \mathbf{n}$,

*kanso@usc.edu

where \mathbf{n} is the normal direction vector, then Eq. (4) becomes

$$\mathbf{r}_t = -\mathbf{r}_{ssss} + (3\theta_s\theta_{ss} + 2\Lambda_s)\mathbf{t} + \Lambda\theta_s\mathbf{n}. \quad (5)$$

Using the inextensibility relation $\mathbf{r}_{ts} \cdot \mathbf{t} = 0$, we obtain that the tension term Λ satisfies the following equation,

$$\Lambda_{ss} - \frac{1}{2}\theta_s^2\Lambda = 3\theta_{ss}^2 + \frac{7}{2}\theta_s\theta_{sss} - \frac{1}{2}\theta_s^4. \quad (6)$$

At the clamped base $s = 0$, we have $\mathbf{r}_t(s = 0, t) = \mathbf{0}$, we obtain one boundary condition that $\Lambda_s = -3\theta_s\theta_{ss}$. At the free tip $s = 1$, $\Lambda = -F$, where tension is negative when the filament is under compression. We further reduce the dimension by assuming small deformation, under which we have $s \approx x$, $\sin \theta \approx \theta \approx dy/dx$. Take the dot product of Eq. (5) with \mathbf{e}_y and ignore the higher order terms; the equation simplifies to

$$y_t = -y_{xxxx} + 2\Lambda_x y_x + \Lambda y_{xx}. \quad (7)$$

Similarly, Eq. (6) simplifies to $\Lambda_{xx} = 0$. To satisfy the boundary conditions that $\Lambda_x|_{x=0} = 0$, $\Lambda|_{x=1} = -F$, Λ is equal to $-F$ for all x . The clamped boundary condition is given by

$$y|_{x=0} = 0, \quad y_x|_{x=0} = 0, \quad y_{xx}|_{x=1} = 0, \quad y_{xxx}|_{x=1} = 0. \quad (8)$$

Now Eq. (7) is linear, and if we solve it for large F , we obtain oscillation solution with growing amplitude. As we need saturated waveform, we consider nonlinear effect which counterbalance the growing amplitude. We control the curvature and modify the tension as $\Lambda = -F + \alpha y_{xx}^2$. This modification does not change the frequency of oscillation, only its amplitude which depends on the coefficient α ; larger α leads to smaller oscillation amplitude.

We solve Eq. (7) using a finite difference method. For convenience, we write it as

$$y_t = -y_{xxxx} + G(y), \quad (9)$$

where $G(y) = 2\Lambda_x y_x + \Lambda y_{xx}$. We first apply backward Euler to march one time step only,

$$\frac{y^{(k+1)} - y^{(k)}}{dt} = -y_{xxxx}^{(k+1)} + G\left(y^{(k)}\right), \quad (10)$$

where dt is the time step size and $y^{(k)}$ represents the solution at k th time step. For the rest, we apply a second order accuracy backward method [4],

$$\frac{3y^{(k+1)} - 4y^{(k)} + y^{(k-1)}}{2dt} = -y_{xxxx}^{(k+1)} + G\left(2y^{(k)} - y^{(k-1)}\right). \quad (11)$$

The filament is uniformly discretized into M segments with nodes x_1, x_2, \dots, x_{M+1} , and the deflection is accordingly y_1, y_2, \dots, y_{M+1} . The derivatives are calculated by central difference method,

$$\begin{aligned} y_x(x_m) &= \frac{1}{2dx} (-y_{m-1} + y_{m+1}), \\ y_{xx}(x_m) &= \frac{1}{dx^2} (y_{m-1} - 2y_m + y_{m+1}), \\ y_{xxx}(x_m) &= \frac{1}{dx^3} (y_{m-2} - 4y_{m-1} + 6y_m - 4y_{m+1} + y_{m+2}), \end{aligned} \quad (12)$$

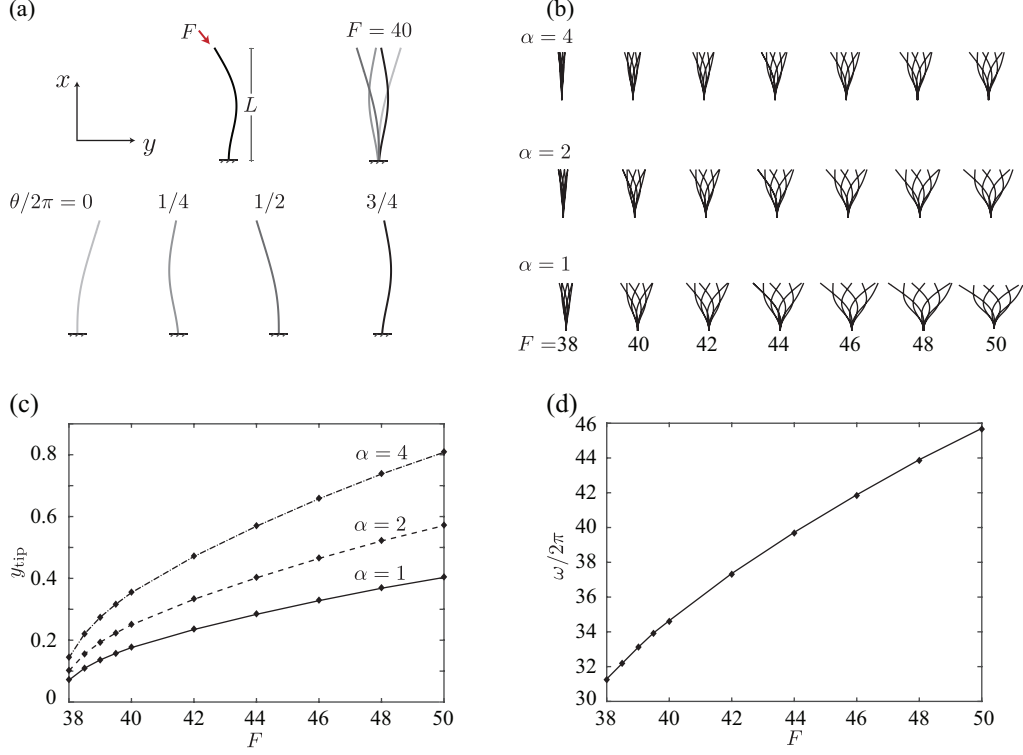


Figure S1: (a) schematic of the filament model (top left): a filament of total length L is clamped to the wall at its base, and it is subject to a follower force of magnitude F at its tip. The steady state beating pattern of the filament for $F = 40$ (top right), with darker color corresponding to increase in phase. Details of the configurations of the filament are shown at four different phase: $\theta/2\pi = 0, 1/4, 1/2$ and $3/4$ (bottom). (b) The beating patterns by varying the activity level F from 38 to 50 and the nonlinear coefficient α such that $\alpha = 1, 2$ and 4 . (c) The largest amplitude at tip as a function of F with $\alpha = 1, 2$ and 4 . (d) The beating frequency as a function of F . The lines corresponding to $\alpha = 1, 2$ and 4 overlap, indicating no dependence of frequency on α .

where the spacial difference size dx is $1/M$. The boundary conditions in Eq. (8) are discretized as

$$\begin{aligned}
 y_1 &= 0, \quad \frac{1}{2dx} (-3y_1 + 4y_2 - y_3) = 0, \\
 \frac{1}{dx^2} (-y_{M-2} + 4y_{M-1} - 5y_M + 2y_{M+1}) &= 0, \\
 \frac{1}{2dx^3} (3y_{M-3} - 14y_{M-2} + 24y_{M-1} - 18y_M + 5y_{M+1}) &= 0.
 \end{aligned} \tag{13}$$

In all simulations, we use $dt = 10^{-5}$ and $dx = 0.01$. When the follower force passes $F = 37.5$, the filament undergoes oscillatory motion. Fig. S1(a) shows the filament's steady-state waveform when $F = 40$ and $\alpha = 4$. We write the limit-cycle solution as

$$y(x, t) = y_0(x, \theta(t)), \quad \theta_t = \omega. \tag{14}$$

Here, we define a phase parameter θ and the beating frequency ω . The solution has a period of 2π that $y_0(s, \theta + 2\pi) = y_0(s, \theta)$. We define $\theta = 0$ when the filament tip reaches the largest amplitude along the positive y direction. Fig. S1(a) also plots the configurations in one period at $\theta/2\pi = 0$,

1/4, 1/2, 3/4. By varying F from 38 to 50, and α from 1 to 4. We obtain a set of waveforms in Fig. S1(b). The amplitude increases as F increases and α decreases. In Fig. S1(c) and (d), we plot the tip amplitude and the frequency as functions of F . Both amplitude and frequency increase as F increases, while the frequency is independent of α .

2 Two hydrodynamically-coupled filaments

For two filaments coupled via fluid, the force balance equation is modified as

$$\mathbf{f}_h^{(i)} + \mathbf{f}_h^{(j \rightarrow i)} + \mathbf{f}_e^{(i)} = \mathbf{0}, \quad (15)$$

where $i, j = 1, 2$, which represent filament #1 and filament #2; $\mathbf{f}_h^{(j \rightarrow i)}$ is the force exerted by filament # j on filament # i through fluid, which is proportional to the velocity field induced by filament # j ,

$$\mathbf{f}_h^{(j \rightarrow i)} = \xi \left(\mathbf{I} - \frac{1}{2} \mathbf{t}^{(i)} \mathbf{t}^{(i)} \right) \cdot \mathbf{v}^{(j \rightarrow i)}. \quad (16)$$

For a slender filament, the flow field due to its motion is approximated by that induced by a line of Stokeslets distributed along the centerline. Then $\mathbf{v}^{(j \rightarrow i)}$ is represented by an integral

$$\mathbf{v}^{(j \rightarrow i)}(s) = -\frac{1}{8\pi\mu} \int_0^1 \left(\frac{\mathbf{I}}{|\mathbf{r}^{(i)}(s) - \mathbf{r}^{(j)}(s')|} + \frac{[\mathbf{r}^{(i)}(s) - \mathbf{r}^{(j)}(s')][\mathbf{r}^{(i)}(s) - \mathbf{r}^{(j)}(s')]}{|\mathbf{r}^{(i)}(s) - \mathbf{r}^{(j)}(s')|^3} \right) \cdot \mathbf{f}_h^{(j)}(s') ds'. \quad (17)$$

In this study, we apply an asymptotic expression of $\mathbf{v}^{(j \rightarrow i)}$ based on the analysis in Ref. [5, 6, 7]. The asymptotic study took advantage of a biologically-relevant length separation that $a \ll h \ll L$, where a is the filament radius and h is the interfilamentous distance. Eq. (17) is simplified as

$$\mathbf{v}^{(j \rightarrow i)}(s) = \frac{1}{4\pi\mu} \ln \frac{h}{L} (\mathbf{I} + \mathbf{e}_x \mathbf{e}_x) \cdot \mathbf{f}_h^{(j)}(s). \quad (18)$$

Under the assumption of small deformation and weak coupling, $\mathbf{f}_h^{(j)} \approx -\xi y_t^{(j)} \mathbf{e}_y$, taking $\xi = 4\pi\mu/\ln(L/a)$, $\mathbf{v}^{(j \rightarrow i)} \approx \ln(L/h)/\ln(L/a) y_t^{(j)} \mathbf{e}_y$. Here, we define a geometric coefficient, $\gamma = \ln(L/h)/\ln(L/a)$, to indicate the coupling strength. As $a \ll h$, γ is always smaller than 1. Following the same procedure of nondimensionalization in Section 1, the reduced-order equations for the two hydrodynamically-coupled filaments are ($i = 1, 2$)

$$y_t^{(i)} - \gamma y_t^{(j)} = -y_{xxxx}^{(i)} + 2\Lambda_x^{(i)} y_x^{(i)} + \Lambda^{(i)} y_{xx}^{(i)}. \quad (19)$$

We solve Eq. (19) numerically using the same discretization method. By varying the follower force F , coupling strength γ and the initial phases $\theta_0^{(i)}$, we obtain different modes of synchronization. In Fig. S2, we show four examples numbered I to IV: cases I and II converge to in- and anti-phase synchrony respectively, while cases III and IV achieve nontrivial synchronized states. In III, the amplitudes of two filaments no longer converge to same value, and the phase difference is slightly diverted from π ; while in IV, the amplitudes are almost identical, and the phase difference is between 0 and π .

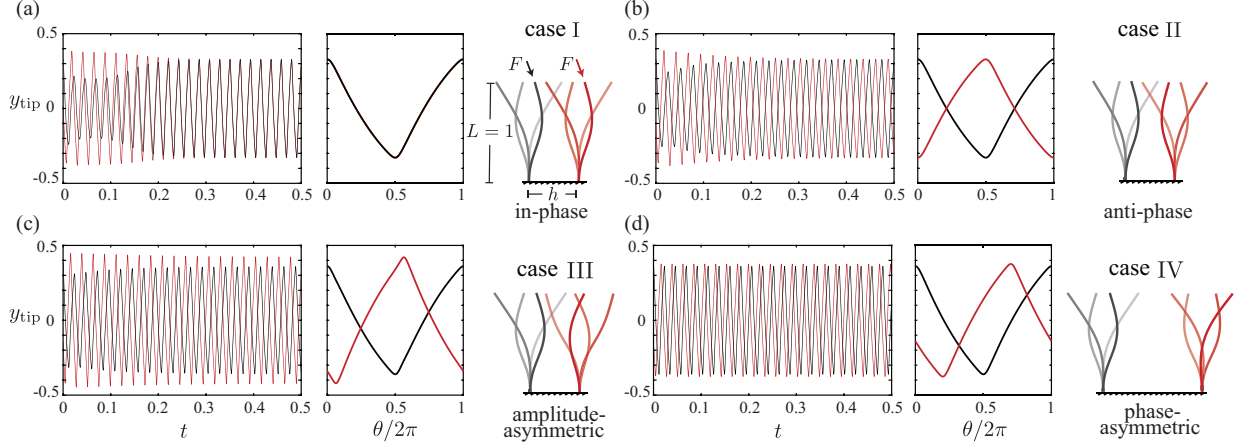


Figure S2: Multiple synchronization modes between two active microfilaments. In all panels, black line represents filament #1 and red line represents filament #2. By varying active force F , coupling strength γ and initial phase difference $\Delta\theta_0$, four distinct synchronous dynamics are presented in: (a) in-phase for $F = 46$, $\gamma = 0.1$, $\Delta\theta_0/2\pi = 0.2$; (b) anti-phase for $F = 46$, $\gamma = 0.1$, $\Delta\theta_0/2\pi = 0.3$; (c) asymmetric synchronization for $F = 49$, $\gamma = 0.1$, $\Delta\theta_0/2\pi = 0.3$, the amplitude of filament #2 is larger than that of filament #1; (d) asymmetric synchronization for $F = 48$, $\gamma = 0.01$, $\Delta\theta_0/2\pi = 0.3$, the phase difference between two filaments is between 0 and π . In each panel, the left plots show the filament tip positions from $t = 0$ until convergence; middle plots show the steady state oscillations of the tip position over one period of oscillation with respect to the phase parameter $\theta/2\pi$; right plots show the filaments motion over one period of oscillation. Most faded color is applied for $\theta = 0$ and the darker corresponds to increase in time. We mark these four cases as I, II, III, IV.

3 Hydrodynamic Force Analysis

We calculate the hydrodynamic forces acting on the coupled filaments in Fig. S2 corresponding to $F = 46$, 49 and 48, respectively. We first study the force on a single filament. In Fig. S3(a-c), we plot the distribution of hydrodynamic forces along the filament, shown in red arrows, for $F = 46$, 49, and 48, respectively, at phases $\theta = 0, \pi/4, \pi/2$ and $3\pi/4$. In Fig. S3(d-e), we integrate the x - and y - components of the force along the filament and plot the resulting components F_x and F_y of the net force as a function of phase θ . The instantaneous values of the net transverse force F_y are much larger than those of the longitudinal force F_x . However, the time-averaged transverse force \bar{F}_y is identically zero while the time-averaged longitudinal \bar{F}_x (or propulsive force) is negative with magnitudes equal to 3.18, 4.50, and 4.05 for $F = 46$, 49 and 48, respectively.

In Fig. S4, we calculate the net hydrodynamic forces on the coupled filaments of Fig. S2. Compared to the single filament, the propulsive force acting on each filament remains the same during in-phase and anti-phase synchronization (Fig. S4(a-b)). The non-trivial synchronization modes lead to asymmetry in force generation. Note that during in-phase, $y^{(1)} = y^{(2)}$, and the hydrodynamic force on filament # i is linear in $(1 - \gamma)y_t^{(i)}$. Compared to the single filament, the beating velocity increases as $y_t^{(i)} = (1 - \gamma)^{-1}y_t^{(0)}$. As a result, the force is unchanged by hydrodynamic coupling. The anti-phase synchronization can be similarly explained. In Fig. S4(c), with $F = 49$ and $\gamma = 0.1$, the propulsive force on filament #1 decreases by about 12% and increased about 11% on filament #2. In Fig. S4(d), with $F = 48$ and $\gamma = 0.01$, the propulsive force on filament #1 decreases by about 3.7% while #2 increases by about 3.6%.

The results in Fig. S4 indicate that (i) the hydrodynamic force on each filament during in- and anti-phase synchrony is unchanged compared to that of a single filament, (ii) asymmetric synchrony produces asymmetric forces that could result in a net moment on the filament pair, and

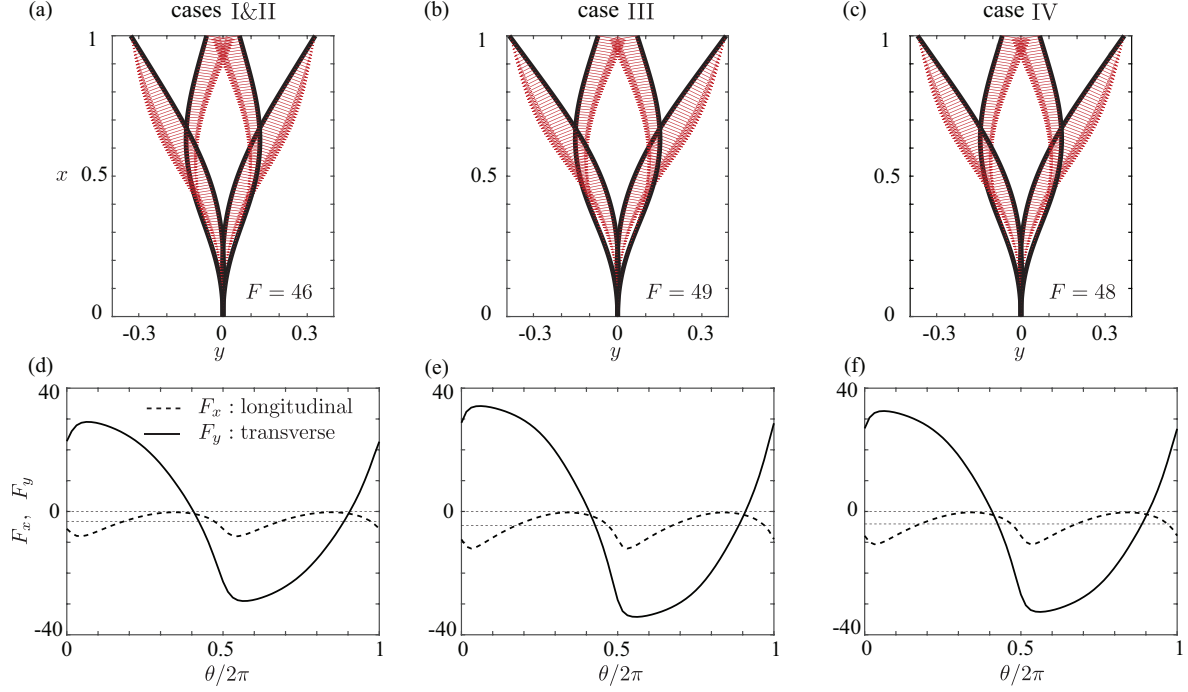


Figure S3: (a-c) Distribution of hydrodynamic forces along the filament at phase $\theta = 0, \pi/4, \pi/2$ and $3\pi/4$, for active force $F = 46, 49$ and 48 corresponding to the cases I-IV of Fig. S2, filament centerline shown in black and forces in red arrows. (d-f) Net force components $F_{x,y}$, integrated along the filament, as a function of phase. Time-averaged force components $\bar{F}_{x,y}$ are shown in gray dash lines. The average transverse force \bar{F}_y is identically zero, and the longitudinal force \bar{F}_x is negative, with magnitude 3.18, 4.50 and 4.05 for active force $F = 46, 49$ and 48 , respectively.

(iii) the total hydrodynamic force on both filaments is independent of the synchronization mode and coupling strength γ . The findings in Fig. S4 raise several hypotheses on the force generation and its impact on locomotion, specifically, regarding the tradeoffs between stability of forward swimming and tumbling motions [8]. These questions will be explored in future work that combines flagella beating motions to a free-swimming cell body.

4 Floquet Multipliers

Eq. (19) has two easily-observable equilibria, corresponding to in-phase and anti-phase synchronizations. In-phase state is given by

$$y^{(1)} = y^{(2)} = y_0(s, \theta), \quad \theta_t = (1 - \gamma)^{-1}\omega, \quad (20)$$

and anti-phase state

$$y^{(1)} = -y^{(2)} = y_0(s, \theta), \quad \theta_t = (1 + \gamma)^{-1}\omega. \quad (21)$$

In both in-phase and anti-phase states, the filaments maintain the same beating pattern with that of the single filament, with the exception that the coupled filaments beat faster for in-phase synchrony and slower for anti-phase synchrony.

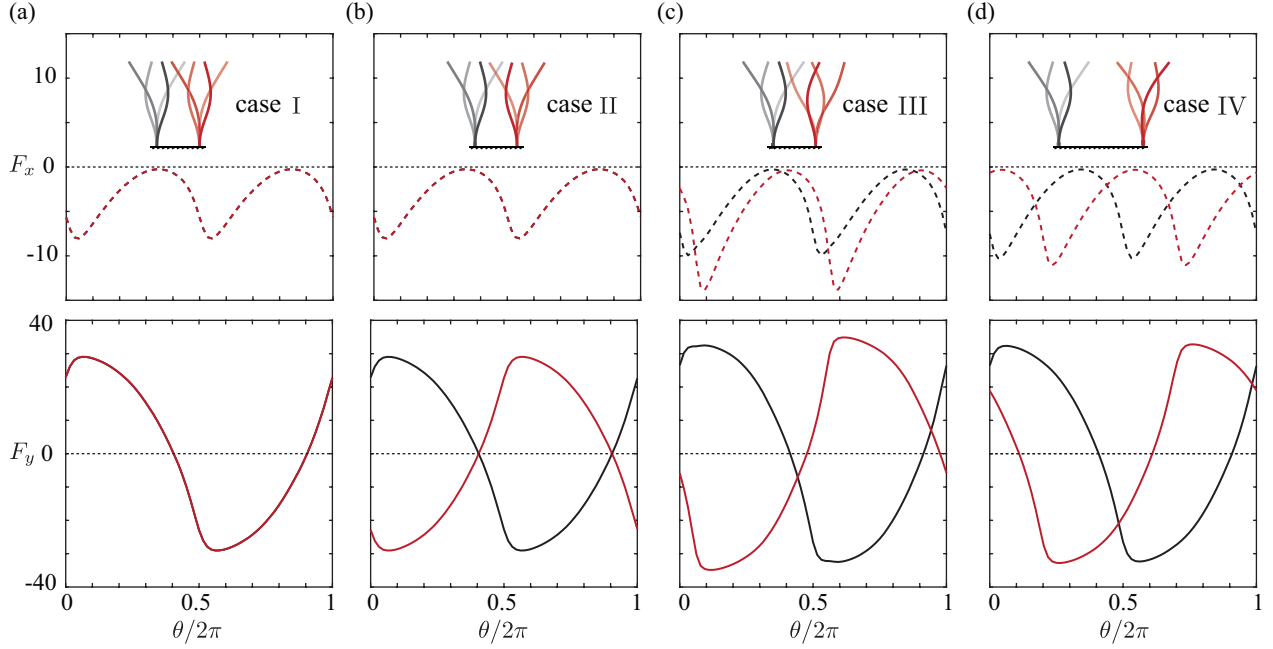


Figure S4: Net hydrodynamic force corresponding to case I (a), II (b), III (c) and IV (d) of Fig. S2. The longitudinal components F_x are shown in dash lines in the upper row, and the transverse components F_y are shown in solid lines in the lower row. In each plot, black represents the force on filament #1 and red on # 2. The average longitudinal forces are: (a) $\bar{F}_{1x} = \bar{F}_{2x} = -3.19$; (b) $\bar{F}_{1x} = \bar{F}_{2x} = -3.18$; (c) $\bar{F}_{1x} = -3.95$, $\bar{F}_{2x} = -5.00$; (d) $\bar{F}_{1x} = -3.90$, $\bar{F}_{2x} = -4.20$.

In terms of the phase variables $\theta^{(1)}$ and $\theta^{(2)}$, in-phase and anti-phase synchrony correspond to two orbits, given by $\theta^{(1)} = \theta^{(2)}$ and $\theta^{(1)} = \theta^{(2)} + \pi$. We first linearize the system around in-phase synchrony.

Considering small perturbations around the in-phase synchrony, $y^{(i)} = y_0 + \delta y^{(i)}$, the perturbations $\delta y^{(i)}$ satisfy

$$\delta y_t^{(i)} - \gamma \delta y_t^{(j)} = \mathcal{L}(y^{(i)}), \quad (22)$$

where the linear operator \mathcal{L} is

$$\mathcal{L}(y; y_0) = -y_{xxxx} + 2[(-F + \alpha y_{0xx}^2)y_x + 2\alpha y_{0x}y_{0xx}y_{xx}]_x - (-F + 3\alpha y_{0xx}^2)y_{xx}. \quad (23)$$

Taking difference of Eq. (22) in the amplitude, we introduce the amplitude difference $\delta y^- = \delta y^{(1)} - \delta y^{(2)}$; it satisfies

$$(1 + \gamma)\delta y_t^- = \mathcal{L}[\delta y^-; y_0(s, (1 - \gamma)^{-1}\omega t)]. \quad (24)$$

Further, we use $\theta = (1 - \gamma)^{-1}\omega t$ to rescale time; Eq. (24) becomes

$$\frac{1 + \gamma}{1 - \gamma}\omega(F)\delta y_\theta^- = \mathcal{L}[\delta y^-; y_0(s, \theta; F)]. \quad (25)$$

Similarly, for anti-phase synchrony, we consider $y^{(i)} = \pm y_0 + \delta y^{(i)}$, and $\delta y^+ = \delta y^{(1)} + \delta y^{(2)}$, the corresponding linearized equation is

$$\frac{1 - \gamma}{1 + \gamma}\omega(F)\delta y_\theta^+ = \mathcal{L}[\delta y^+; y_0(s, \theta; F)]. \quad (26)$$

By solving the single filament problem, we obtain the limit-cycle solution $y_0(x, \theta)$. Then using the same discretization and time-stepping scheme in section 1, we integrate Eq. (25) and (26) for one period to get the Floquet multipliers. For convenience, we rewrite Eq. (25) and (26) as

$$C\omega\delta y_\theta = \mathcal{L}[\delta y], \quad (27)$$

where $C = (1 + \gamma)/(1 - \gamma)$ for the equation linearized around in-phase synchrony and $C = (1 - \gamma)/(1 + \gamma)$ for that linearized around anti-phase synchrony. Since we have solved for y_0 , then the frequency ω at equilibrium is known. The solution is discretized into $\delta y_1, \delta y_2, \dots, \delta y_{M+1}$ at the positions x_1, x_2, \dots, x_{M+1} . Considering the clamped boundary conditions, we have

$$\begin{aligned} \delta y_1 &= 0, \quad \delta y_2 = \frac{1}{4}\delta y_3, \\ \delta y_M &= \frac{1}{11}(28\delta y_{M-1} - 23\delta y_{M-2} + 6\delta y_{M-3}), \\ \delta y_{M+1} &= \frac{1}{11}(48\delta y_{M-1} - 52\delta y_{M-2} + 15\delta y_{M-3}). \end{aligned} \quad (28)$$

Since $\delta y_{1,2,M,M+1}$ depend on $\delta y_{3,\dots,M-1}$, we define a column vector $\delta \mathbf{y} = [\delta y_3, \delta y_4, \dots, \delta y_{M-1}]^T$. Thus, in discrete form, Eq. (27) becomes a set of ordinary different equations,

$$\delta \mathbf{y}_\theta = \mathbf{A}(\theta)\delta \mathbf{y}, \quad (29)$$

where \mathbf{A} is a periodic matrix with period 2π . For this type of problem, the solution has the form that

$$\delta \mathbf{y}(\theta) = e^{\mu\theta} \mathbf{p}(\theta), \quad (30)$$

where \mathbf{p} has period 2π . Let $\delta \mathbf{y}^{(i)}$ be $M-3$ independent solutions of Eq. (29), a fundamental matrix \mathbf{Y} is defined as

$$\mathbf{Y}(\theta) = [\delta \mathbf{y}^{(1)}, \delta \mathbf{y}^{(2)}, \dots, \delta \mathbf{y}^{(M-3)}]. \quad (31)$$

The fundamental matrix satisfies that

$$\mathbf{Y}(\theta + 2\pi) = \mathbf{Y}(\theta)\mathbf{B}, \quad (32)$$

where \mathbf{B} is a constant matrix. The eigenvalues $\rho^{(i)}$ of \mathbf{B} are called Floquet multipliers, that indicate the growth rate of the system $\rho^{(i)} = e^{2\pi\mu^{(i)}}$. Numerically, to compute \mathbf{B} , we set $M-3$ independent initial conditions

$$\delta \mathbf{y}_0 = \mathbf{e}^{(i)}, \quad i = 1, 2, \dots, M-3, \quad (33)$$

where the entries of the vector $\mathbf{e}^{(i)}$ are all zero except the i th entry, it is equal to 1. For each set $\mathbf{e}^{(i)}$ of initial conditions, we integrate Eq. (27) numerically, using the discretization scheme described above, for one period in time. We obtain $M-3$ solutions $\mathbf{b}^{(i)}$ corresponding to $M-3$ initial conditions $\mathbf{e}^{(i)}$, which we write in matrix form,

$$\mathbf{B} = [\mathbf{b}^{(1)}, \dots, \mathbf{b}^{(M-3)}]. \quad (34)$$

The Floquet multipliers are the eigenvalues of \mathbf{B} , and the dominant one is the Floquet multiplier with the largest magnitude $|\rho|$.

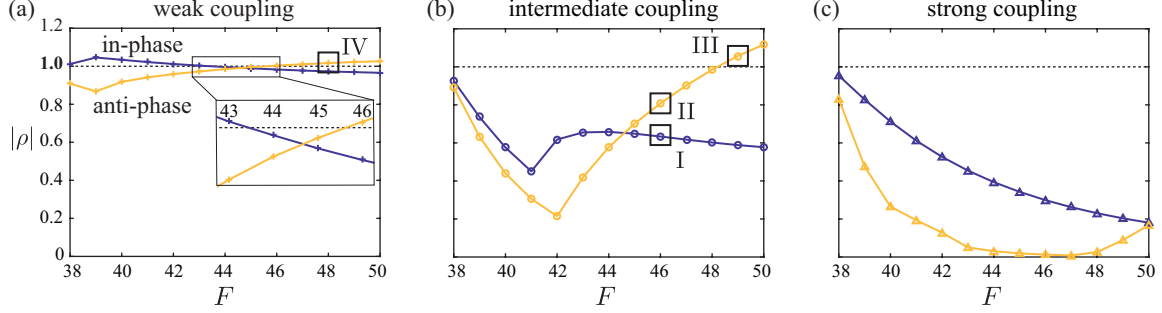


Figure S5: Floquet multipliers correspond to in-phase (blue) and anti-phase (yellow) synchrony in three cases: (a) Weak coupling for $\gamma = 0.01$; (b) Intermediate coupling for $\gamma = 0.1$; (c) Strong coupling for $\gamma = 0.33$. The boxed values I to IV correspond to the four cases of synchrony in FIG. S2.

In Fig. S5, we calculate the values of $|\rho|$ for the same parameter spaces considered with Fig. 2 of the main text, for weak, intermediate and strong coupling. We show the values of $|\rho|$ corresponding to in-phase in blue, and those to anti-phase in yellow. For weak coupling (Fig. S5(a)), in-phase synchrony transitions from unstable to stable at some value of F between 43 and 44, and anti-phase transitions from stable to unstable for F somewhere between 45 and 46. This is in good agreement with the nonlinear simulations, which shows that both transitions occur roughly between 44 and 45. It is also interesting to link the nonlinear simulations to Eq. (25) and (26) when γ is very small. The values of the dominant Floquet multiplier are around $|\rho| = 1$, which corresponds to the case without hydrodynamic coupling and two filaments beat independently. At intermediate coupling (Fig. S5(b)), in-phase is always stable while anti-phase become unstable when $F > 48$. In strong coupling case, both in-phase and anti-phase states are always stable. Fig. S5(b) and (c) are exactly consistent with the nonlinear simulations.

5 Kuramoto-style Analysis

In this section, we analyze the stability of the multi-modes of synchrony under the assumption of weak coupling. In this limit, the dynamics of the two filaments follow the single filament solution, albeit at different phases.

For notational convenience, we write the righthand-side of Eq. (7) as a nonlinear operator $\mathcal{N}[y]$. For a given follower force F and the coupling strength γ , the steady-state oscillatory solution $y_0(x, t)$ satisfies

$$y_{0t}(x, t) = \mathcal{N}[y_0(x, t)], \quad (35)$$

where $\mathcal{N}[y] = -y_{xxxx} + 2\Lambda_x y_x + \Lambda y_{xx}$. If we write the limit-cycle solution y_0 as a function of phase θ and introduce the function $u_0(x, \theta) = y_{0\theta}(x, \theta) = \partial y_0 / \partial \theta$, Eq. (35) becomes

$$\omega u_0(x, \theta) = \mathcal{N}[y_0(x, \theta)]. \quad (36)$$

For notational convenience, we will hide the space variable x in the following calculations. For two filaments, we write Eq. (19) as

$$y_t^{(i)}(t) - \gamma y_t^{(j)}(t) = \mathcal{N}[y^{(i)}(t)]. \quad (37)$$

Using $\theta^{(i)}$ to represent the phase of filament $\#i$ at time t , Eq. (37) becomes

$$\theta_t^{(i)} u^{(i)}(\theta^{(i)}) - \gamma \theta_t^{(j)} u^{(j)}(\theta^{(j)}) = \mathcal{N}[y^{(i)}(\theta^{(i)})], \quad (38)$$

where we define $u^{(i)}(\theta) = \partial y^{(i)} / \partial \theta^{(i)}$. When γ is small (weak coupling), the orbit of each filament in the solution space is only slightly perturbed around the orbit of an isolated filament. Taking advantage of weak coupling, we apply the asymptotic approximations that

$$y^{(i)}(\theta) \approx y_0(\theta^{(i)}), \quad u^{(i)}(\theta) \approx u_0(\theta^{(i)}). \quad (39)$$

Substituting Eq. (39) into Eq. (38), and applying Eq. (36) we obtain

$$\theta_t^{(i)} u_0(\theta^{(i)}) - \gamma \theta_t^{(j)} u_0(\theta^{(j)}) = \omega u_0(\theta^{(i)}). \quad (40)$$

Rearranging and neglecting higher order terms in γ , we have

$$\theta_t^{(i)} u_0(\theta^{(i)}) = \omega u_0(\theta^{(i)}) + \gamma \omega u_0(\theta^{(j)}). \quad (41)$$

In the solution space, u_0 represents the tangent of the orbit of the periodic solution y_0 of a single filament. Taking derivative of Eq. (36) with respect to θ , we find that u_0 is the eigenfunction, associated with zero eigenvalue, of the linear operator $\mathcal{J} = (\mathcal{L} - \omega \frac{\partial}{\partial \theta})$, where \mathcal{L} is given by Eq. (23), such that

$$\mathcal{J}[u_0] = \left(\mathcal{L} - \omega \frac{\partial}{\partial \theta} \right) [u_0] = 0. \quad (42)$$

We introduce a normalized adjoint function \hat{u}_0 which satisfies

$$\int_0^1 u_0(\theta) \hat{u}_0(\theta) dx = 1. \quad (43)$$

We follow the method in Ref. [9] to derive the adjoint function. We define an inner product of functions u and \hat{u} ,

$$\langle u, \hat{u} \rangle = \frac{1}{2\pi} \int_0^{2\pi} d\theta \int_0^1 u \hat{u} dx, \quad (44)$$

such that the adjoint operator $\hat{\mathcal{J}}$ associated with the operator \mathcal{J} satisfies

$$\langle u, \hat{\mathcal{J}}[\hat{u}] \rangle = \langle \hat{u}, \mathcal{J}[u] \rangle. \quad (45)$$

We use integration by parts to find an expression for the differential operator $\hat{\mathcal{J}}$ and the associated boundary conditions. To this end, we substitute the expression of \mathcal{L} in Eq. (23) into Eq. (45); the right hand side of Eq. (45) is

$$\begin{aligned} \langle \hat{u}, \mathcal{J}[u] \rangle = & \frac{1}{2\pi} \int_0^{2\pi} \int_0^1 dx \left(\hat{u} \left\{ -u_{xxxx} + 2[(-F + \alpha y_{0xx}^2)u_x + 2\alpha y_{0x} y_{0xx} u_{xx}]_x \right. \right. \\ & \left. \left. - (-F + 3\alpha y_{0xx}^2)u_{xx} \right\} - \omega \hat{u} u_\theta \right). \end{aligned} \quad (46)$$

We divide the integral into four parts. For the part with \hat{u}_{xxxx} , by integration by parts, we have

$$\int_0^1 \hat{u} u_{xxxx} dx = \int_0^1 u \hat{u}_{xxxx} dx + [\hat{u} u_{xxx} - \hat{u}_x u_{xx} + \hat{u}_{xx} u_x - \hat{u}_{xxx} u] \Big|_{x=0}^{x=1}. \quad (47)$$

Applying the boundary conditions that

$$u|_{x=0} = 0, \quad u_x|_{x=0} = 0, \quad u_{xx}|_{x=1} = 0, \quad u_{xxx}|_{x=1} = 0, \quad (48)$$

Eq. (47) becomes

$$\int_0^1 \hat{u} u_{xxx} dx = \int_0^1 u \hat{u}_{xxx} dx - [\hat{u} u_{xxx} - \hat{u}_x u_{xx}]|_{x=0} + [\hat{u}_{xx} u_x - \hat{u}_{xxx} u]|_{x=1}. \quad (49)$$

Then for the second part, we have

$$\begin{aligned} \int_0^1 dx \hat{u} [(-F + \alpha y_{0xx}^2) u_x + 2\alpha y_{0x} y_{0xx} u_{xx}]_x \\ = - \int_0^1 dx \hat{u}_x [(-F + \alpha y_{0xx}^2) u_x + 2\alpha y_{0x} y_{0xx} u_{xx}] - F \hat{u} u_x|_{x=1}, \\ = \int_0^1 dx u [\hat{u}_x (-F + \alpha y_{0xx}^2)]_x - 2\alpha u (\hat{u}_x y_{0x} y_{0xx})_{xx} + F(-\hat{u} u_x + \hat{u}_x u)|_{x=1}, \end{aligned} \quad (50)$$

where we also applied the boundary conditions for y_0 that

$$y_0|_{x=0} = 0, \quad y_{0x}|_{x=0} = 0, \quad y_{0xx}|_{x=1} = 0, \quad y_{0xxx}|_{x=1} = 0. \quad (51)$$

The third part integral is calculated as

$$\int_0^1 dx \hat{u} (-F + 3\alpha y_{0xx}^2) u_{xx} = \int_0^1 dx u [(-F + 3\alpha y_{0xx}^2) \hat{u}]_{xx} + F [-\hat{u} u_x + \hat{u}_x u]_{x=1}. \quad (52)$$

For the last part we have

$$\int_0^{2\pi} d\theta \hat{u} u_\theta = - \int_0^{2\pi} d\theta \hat{u}_\theta u. \quad (53)$$

Combining Eq. (47), (50), (52), and (53), we have

$$\langle \hat{u}, \mathcal{J}[u] \rangle = \langle u, \hat{\mathcal{J}}[\hat{u}] \rangle + [\hat{u} u_{xxx} - \hat{u}_x u_{xx}]|_{x=0} + [-(\hat{u}_{xx} + F \hat{u}) u_x + (\hat{u}_{xxx} + F \hat{u}_x) u]|_{x=1}, \quad (54)$$

where

$$\hat{\mathcal{J}}[\hat{u}] = \left(\hat{\mathcal{L}} + \omega \frac{\partial}{\partial \theta} \right) [\hat{u}], \quad (55)$$

$$\hat{\mathcal{L}}[\hat{u}] = -\hat{u}_{xxxx} + 2[(-F + \alpha y_{0xx}^2) \hat{u}]_x - [4\alpha y_{0x} y_{0xx} \hat{u}_x + (-F + 3\alpha y_{0xx}^2) \hat{u}]_{xx}. \quad (56)$$

By setting the boundary terms in Eq. (54) to zeros, we obtain boundary conditions

$$\begin{aligned} \hat{u}(0) = 0, \quad \hat{u}_x(0) = 0, \\ [\hat{u}_{xx} + F \hat{u}]_{x=1} = 0, \\ [\hat{u}_{xxx} + F \hat{u}_x]_{x=1} = 0. \end{aligned} \quad (57)$$

We compute the adjoint eigenfunction \hat{u}_0 , associated with the zero eigenvalue, of the adjoint operator $\hat{\mathcal{J}}$, which satisfies

$$\hat{\mathcal{J}}[\hat{u}_0] = 0, \quad (58)$$

where $\hat{\mathcal{J}}$ is given by (55) and (56), together with the boundary conditions in Eq. (57).

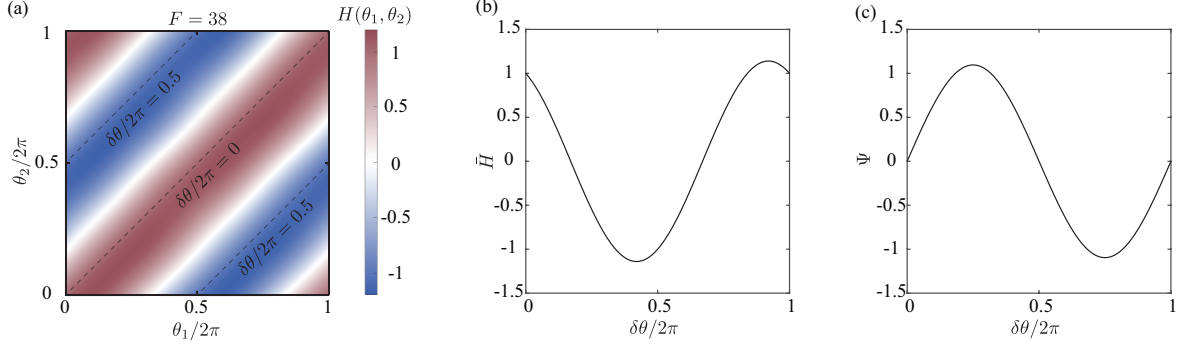


Figure S6: (a) Phase coupling function $H(\theta_1, \theta_2)$ for $F = 38$. (b) Averaged value \bar{H} in a period along the line $\theta_2 = \theta_1 + \delta\theta$. (c) Phase description function $\Psi(\Delta) = \bar{H}(-\Delta\theta) - \bar{H}(\Delta\theta)$.

The adjoint eigenfunction \hat{u}_0 is normalized such that $\int_0^1 u_0(\theta) \hat{u}_0(\theta) dx = 1$. We can prove by taking derivative with respect to θ that,

$$\frac{\partial}{\partial \theta} \int_0^1 u_0(\theta) \hat{u}_0(\theta) dx = \frac{1}{\omega} \int_0^1 \left(\hat{u}_0 \mathcal{L}[u_0] - u_0 \hat{\mathcal{L}}[\hat{u}_0] \right) dx = 0. \quad (59)$$

Next, we project Eq. (41) onto the single filament solution u_0 by taking its inner product with the adjoint function $u_0(\theta^{(i)})$, noting that Eq. (43) holds at each phase. The phase variables follow equations

$$\theta_t^{(i)} = \omega + \gamma \omega \int_0^1 \hat{u}_0(x, \theta^{(i)}) u_0(x, \theta^{(j)}) dx. \quad (60)$$

Here, we define the phase coupling function $H(\theta^{(i)}, \theta^{(j)})$

$$H(\theta^{(i)}, \theta^{(j)}) = \int_0^1 \hat{u}_0(x, \theta^{(i)}) u_0(x, \theta^{(j)}) dx. \quad (61)$$

Then Eq. (60) can be written as

$$\theta_t^{(i)} = \omega \left[1 + \gamma H(\theta^{(i)}, \theta^{(j)}) \right]. \quad (62)$$

Taking difference of Eq. (62) for $i = 1, 2$; the phase difference $\Delta\theta = \theta^{(2)} - \theta^{(1)}$ satisfies,

$$\Delta\theta_t = \gamma \omega \left[H(\theta^{(2)}, \theta^{(1)}) - H(\theta^{(1)}, \theta^{(2)}) \right]. \quad (63)$$

Next we average H along the line $\theta_2 = \theta_1 + \Delta\theta$. As the function is periodic, the averaged value \bar{H} is a function of $\Delta\theta$ only,

$$\bar{H}(\Delta\theta) = \frac{1}{2\pi} \int_0^{2\pi} d\phi H(\theta_1 + \phi, \theta_2 + \phi). \quad (64)$$

Using \bar{H} to approximate H , Eq. (63) becomes

$$\Delta\theta_t = \gamma \omega \left[\bar{H}(-\Delta\theta) - \bar{H}(\Delta\theta) \right]. \quad (65)$$

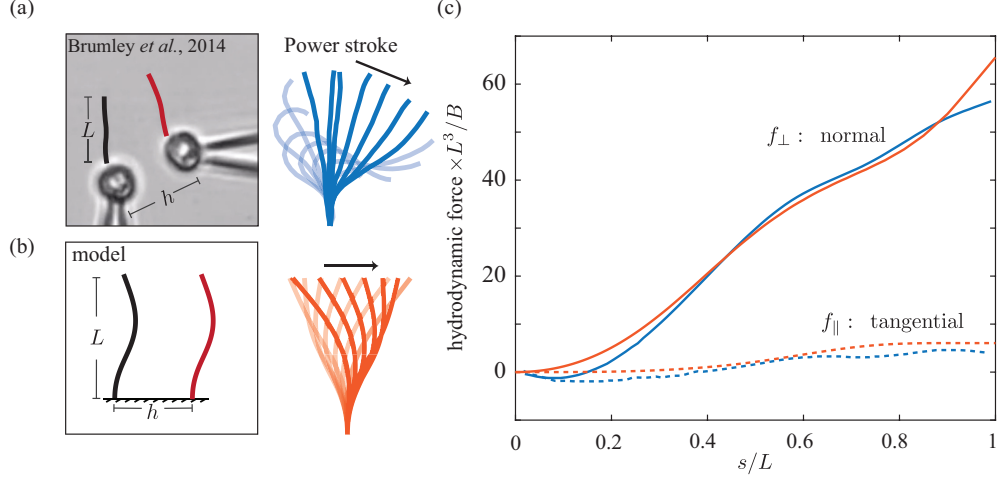


Figure S7: (a) Two isolated somatic cells of *Volvox carteri* with flagellar length L and separation h , and the waveform of a single flagellum (shown in blue). Left and right figures are recreated from Ref. [10, Video 1 and Fig. 4A]. (b) Schematics of the filament model and the waveform of the filament applied by the active force $F = 50$ (shown in orange). (c) Comparison of the normal (solid line) and tangential (dash line) components of the distribution of hydrodynamic force between the experiment (blue) and the model (orange). The blue lines are extracted from Ref. [10, Fig. 4B].

We define $\Psi(\Delta\theta) = \bar{H}(-\Delta\theta) - \bar{H}(\Delta\theta)$ to study dynamics of the phase difference.

Taking $F = 38$ as an example, we calculate $u_0 = \partial y_0 / \partial \theta$, and solve \hat{u}_0 from Eq. (58) with boundary conditions in Eq. (57). Then we calculate $H(\theta_1, \theta_2)$ from Eq. (61) and plot it in Fig. S6(a). According to Eq. (64) and (65), we plot averaged coupling function \bar{H} and the phase function Ψ as functions of phase difference in Fig. S6(b) and (c) respectively. In this case, $\Psi = 0$ when the phase difference is either 0 or π , which indicate the in- and anti-phase synchrony. The stability of the fixed points shows that only anti-phase is stable, which is consistent with the nonlinear simulation (Fig. 1(a) in the main text).

6 Comparison to Experimental Data

Ref. [10] studied two isolated somatic cells of *Volvox carteri* and observed synchronous beating due to hydrodynamic coupling only (Fig. S7a, recreated from Fig. 4A of Ref. [10]). The distance h between the cells had to be small compared to the flagellar length L in order for hydrodynamic coupling to dominate the environmental noise and lead to synchronization. Both in-phase and anti-phase synchronization were observed over a range of separation distances, and a coupling strength κ , which indicates how fast the two flagella reach synchronization, was measured in the experiment. Here, we recreate the original data from Fig. 5A of Ref. [10] in Fig. S8(a), where we applied a colormap and notation that are consistent with our study. In Fig. S8(b), we sample the data into four ranges of κ that we divide evenly in log-space, and in (c) we count the instances of in- and anti-phase synchronization for each range of κ values. Obviously, in-phase and anti-phase synchrony coexists over a wide range of κ values.

Using the time and length scales introduced in the main paper, we calculate the frequency and force of flagellar beat reported in [10] in non-dimensional form. The frequency of the somatic cell of *Volvox carteri* was measured around 30 Hz and the total force was estimated to be around 50 pN [10]. Using the parameters of the cell with length $L = 20\mu\text{m}$ and bending rigidity $B = 4 \times 10^{-22}$

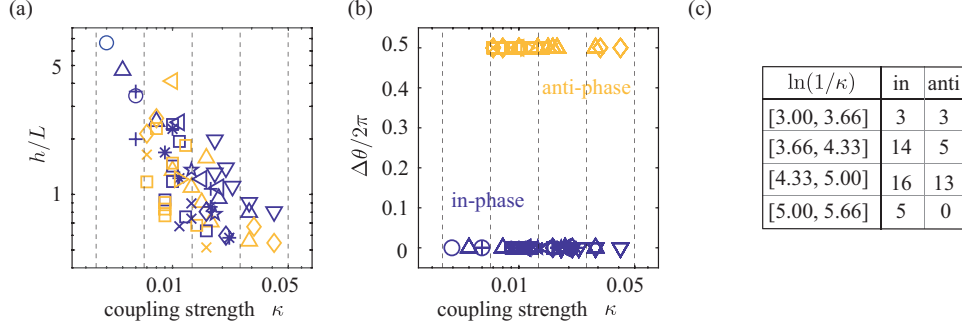


Figure S8: (a) In-phase (blue) and anti-phase (yellow) synchronization observed with different coupling strength κ , recreated from Ref. [10, Fig. 5A], symbols represent different cells. (b) Same data as in (a) represented in terms of phase difference and κ where κ is divided evenly in log-space into four ranges, (c) counting the cases of in- and anti-phase synchronization in each range of κ .

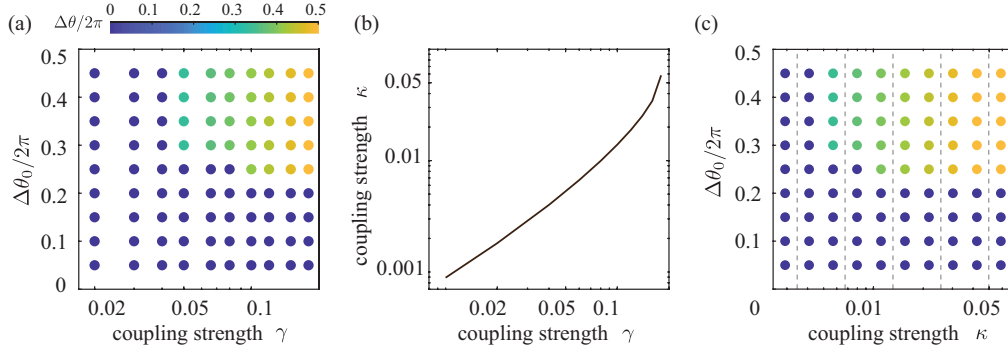


Figure S9: (a) Synchronization modes for $F = 50$ as a function of γ . (b) Mapping between the coupling strength γ in the model and the coupling strength κ in the experiment. (c) Synchronization modes for $F = 50$ as a function of κ .

Nm^2 , we calculate the dimensionless total force to be $F = 50$ and the frequency to be $\omega/2\pi = 48$.

The flagella beat patterns in [10] are characterized by an asymmetric waveform (Fig. S7a) whereas in our filament model, they are symmetric about the vertical (Fig. S7b). Despite this major difference, we computed the oscillations of a single filament subject to an active follower force $F = 50$. The resulting filament frequency is around 46 (Fig. S1d), which is very close to that of the flagellar frequency in [10]. We also calculated the force distribution averaged over half cycle to represent a characteristic force of power stroke. Fig. S7c compares the normal and tangential components of the hydrodynamic force distribution, f_\perp and f_\parallel , along the filament to those obtained based on experimental observations of the flagellum executing its characteristic power stroke (recreated from Fig. 4B of Ref. [10]). Results from the filament model and flagellar system are qualitatively similar.

In Fig. S9a, we show the basins of attraction of the in-phase and anti-phase synchrony for $F = 50$ and various coupling strength γ . Note that here the coupling strength γ has a different definition from κ in [10], but since both determine the coupling strength which immediately affects the dynamics of the phase difference, we can map one to the other. In [10], the coupling strength κ is related to the time scale it takes the two filaments to synchronize. Using the notation of this paper, it is calculated as $-\mu/(2\pi\omega)$, where $-\mu$ is the rate at which the phase evolves towards the corresponding synchronization state. In our study, we examined the stability of the synchronized

states and computed the Floquet multiplier ρ which is less than unity ($\rho < 1$) for stable synchrony and it is related to the (dimensional) decay rate towards the synchronous state via $\mu = \omega \ln \rho / (2\pi)$. Combining the definition of the coupling strength κ in [10], with the Floquet analysis in our paper, we arrive at the following mapping from ρ to κ : $\kappa \sim \ln(1/\rho)/(4\pi^2)$, where ρ depends on F and γ . For $F = 50$, the mapping is shown in Fig. S9(b), and consequently we obtain the basin of attractions as a function of coupling strength κ in Fig. S9(c).

References

- [1] De Canio G, Lauga E, Goldstein RE. Spontaneous oscillations of elastic filaments induced by molecular motors. *J Royal Soc Interface*. 2017;14:20170491.
- [2] Ling F, Guo H, Kanso E. Instability-driven oscillations of elastic microfilaments. *J Royal Soc Interface*. 2018;15:20180594.
- [3] Lighthill J. Flagellar hydrodynamics. *SIAM review*. 1976;18(2):161–230.
- [4] Tornberg AK, Shelley MJ. Simulating the dynamics and interactions of flexible fibers in Stokes flows. *J Comput Phys*. 2004;196:8–40.
- [5] Man Y, Lyndon K, Lauga E. Hydrodynamic interactions between nearby slender filaments. *EPL*. 2016;116:24002.
- [6] Man Y, Page W, Poole RJ, Lauga E. Bundling of elastic filaments induced by hydrodynamic interactions. *Phys Rev Fluids*. 2017;2:123101.
- [7] Goldstein RE, Lauga E, Pesci AI, Proctor MRE. Elastohydrodynamic synchronization of adjacent beating flagella. *Phys Rev Fluids*. 2016;1:073201.
- [8] Polin M, Tuval I, Drescher K, Gollub JP, Goldstein RE. *Chlamydomonas* swims with two “gears” in a eukaryotic version of run-and-tumble locomotion. *Science*. 2009;325(5939):487–490.
- [9] Kawamura T, Tsubaki R. Phase reduction approach to elastohydrodynamic synchronization of beating flagella. *Phys Rev E*. 2018;97:022212.
- [10] Brumley DR, Wan KY, Polin M, Goldstein RE. Flagellar synchronization through direct hydrodynamic interactions. *Elife*. 2014;3:e02750.